Article

Auxetic Laminar Composites Based on P(VDF-TrFE) for Enhanced Piezoelectric Performance in Flexible Energy Devices

Rajiv Kamaraj †, Jen-Hao Chang †, and Yi-Jen Huang *

Department of Chemical and Materials Engineering, National Chin-Yi University of Technology, Taichung 41170, Taiwan
* Correspondence: yjhuang@ncut.edu.tw; Tel.: (+886)-4-2392-4505 (ext. 7508); Fax: (+886)-4-2392-6617
† These authors contributed equally to this work.
Received: 9 October 2025; Revised: 14 November 2025; Accepted: 14 November 2025; Published: 27 November 2025

Abstract: The development of efficient, flexible, and sustainable energy-harvesting technologies is critical for powering self-sufficient wearable electronics, biomedical sensors, and remote IoT systems. In this study, we present an advanced auxetic laminar composite architecture that integrates piezoelectric polymer films—specifically P(VDF-TrFE) and P(VDF-TrFE-CTFE)—with re-entrant honeycomb substrates fabricated using a UV-curable resin. The negative Poisson's ratio (NPR) behavior of auxetic structures was strategically employed to amplify in-plane mechanical strain in the active piezoelectric layers, enhancing voltage output under uniaxial loading. The electrospun nanofibers exhibited uniform, bead-free morphologies with preferential β-phase crystallinity, confirmed via SEM and wide-angle X-ray diffraction (WAXD). Finite element simulations revealed strong stress concentration at re-entrant hinges and vertical struts, with the degree of auxetic deformation increasing at larger monomer angles (55–65°) and thicker substrates. Digital image correlation (DIC) analysis confirmed consistent deformation behavior and validated simulated strain fields. Composite structures incorporating 5 mm-thick auxetic substrates and P(VDF-TrFE) films demonstrated superior mechanical strength, enhanced interfacial stress transfer, and significantly improved voltage response compared to P(VDF-TrFE-CTFE)-based systems. Experimental results showed that induced piezoelectric voltage increased nonlinearly with applied force and excitation frequency, with P(VDF-TrFE) achieving up to ~250% output enhancement. Simulated voltage outputs were in close agreement with experimental trends, supporting the design rationale. This work demonstrates a scalable, low-toxicity, and recyclable design for flexible piezoelectric harvesters using mechanical metamaterials. The integration of auxetic geometries with optimized piezoelectric polymers enables high sensitivity and tunable mechanical-electrical coupling, aligning with sustainable development goals. These findings provide valuable insights for designing next-generation flexible power sources for green energy applications.

Keywords: auxetic structures; piezoelectric polymers; flexible energy harvesting; P(VDF-TrFE); digital image correlation

1. Introduction

The global transition toward sustainable and decentralized energy systems has accelerated research in flexible and scalable energy-harvesting technologies. Among various transduction mechanisms, piezoelectricity has garnered significant interest due to its ability to convert mechanical energy into electrical output without requiring external power sources [1]. This property is particularly advantageous for powering self-sustained devices in applications such as wearable electronics [2], biomedical monitoring [3], remote sensing [4], and the Internet of Things (IoT) [5]. The core challenge, however, lies in developing energy harvesters that are not only efficient and durable but also mechanically compliant, lightweight, and compatible with sustainable manufacturing processes [6].

Conventional piezoelectric materials like $Pb(Zr_xTi_{1-x})O_3$ (PZT) offer high electromechanical coupling but suffer from several drawbacks, including brittleness [7], toxicity [8], and poor compatibility [9] with flexible substrates [10]. In contrast, piezoelectric polymers such as poly(vinylidene fluoride) (PVDF) [11] and its copolymers—particularly poly(vinylidene fluoride-trifluoroethylene) [P(VDF-TrFE)] [12] and poly(vinylidene fluoride-trifluoroethylene-chlorotrifluoroethylene) [P(VDF-TrFE-CTFE)] [13]—have emerged as leading candidates for flexible and wearable energy devices [14]. These fluoropolymer-based materials exhibit intrinsic

Copyright: © 2025 by the authors. This is an open access article under the terms and conditions of the Creative Commons Attribution (CC BY) license (https://creativecommons.org/licenses/by/4.0/).
Publisher's Note: Scilight stays neutral with regard to jurisdictional claims in published maps and institutional affiliations.

flexibility, moderate piezoelectric coefficients, low dielectric loss, and high mechanical strength, making them ideal for conformal energy harvesters [15,16]. Furthermore, they are processable at relatively low temperatures and can be fabricated via spin-coating [17], inkjet printing [18], screen-printing [19], or electrospinning [20], enhancing their scalability and compatibility with green manufacturing techniques [21].

Despite their advantages, one of the main limitations of polymer-based piezoelectric devices is their relatively low piezoelectric output compared to their ceramic counterparts [22]. Recent studies have shown that device architecture and structural mechanics play a crucial role in determining the effective electromechanical coupling of piezoelectric films [23]. Specifically, engineered microstructures can significantly amplify strain localization in active layers, thereby enhancing charge generation [24]. One of the most promising approaches in this context involves the use of auxetic structures—mechanical metamaterials that exhibit a negative Poisson's ratio (NPR), meaning they expand laterally when stretched longitudinally [25].

Auxetic structures have been widely explored in biomedical scaffolds [26], protective equipment [27], and actuators due to their superior toughness [28], energy absorption [29], and deformation characteristics [30]. In the field of piezoelectric energy harvesting, their unique ability to amplify strain under uniaxial loading offers a strategic pathway to boost the local deformation of the piezoelectric film without requiring higher external loads [31]. By embedding piezoelectric films within or on top of re-entrant or NPR substrates, the mechanical strain imparted during actuation can be transferred more effectively into the active layer, thereby improving voltage output and sensitivity [32].

Theoretical models and simulations have supported the efficacy of auxetic geometries in stress concentration and strain amplification [33]. For example, the Trigonometric Zigzag Theory and other analytical approaches have illustrated how re-entrant honeycomb lattices concentrate mechanical energy at hinge points [34], especially as the monomer angle approaches 60–70° [35]. This stress focusing effect can be tuned through design parameters such as lattice angle [36], unit cell size [37], and substrate thickness [38]. Yet, translating these predictions into practical energy harvesting systems remains a challenge due to fabrication constraints, variability in mechanical bonding, and nonlinear effects introduced by polymer film mechanics [39].

Moreover, the interaction between the piezoelectric film and the auxetic substrate introduces complex interfacial behaviors that govern device performance [40]. Issues such as delamination, interfacial strain mismatch, and mechanical damping can limit voltage generation if not properly addressed [41]. Therefore, it is critical to investigate not only the geometrical design but also the material compatibility and mechanical integrity of the film–substrate interface.

In this work, we present a comprehensive experimental and computational investigation of auxetic laminar composite structures based on P(VDF-TrFE) and P(VDF-TrFE-CTFE) films, aimed at enhancing piezoelectric response for flexible energy harvesting. The composite structures incorporate re-entrant geometries with varying monomer tilt angles (55°, 60°, 65°), fabricated using a thermosetting polymer resin as the substrate material. By bonding piezoelectric thin films to substrates of controlled auxetic architecture and systematically varying the design parameters, we investigate how geometric tuning influences mechanical stress transfer and electrical output.

Our approach combines finite element simulations, using detailed stress and displacement analyses, with experimental validation via digital image correlation (DIC) and voltage response measurements under cyclic loading. We further explore the role of polymer copolymerization by comparing P(VDF-TrFE) and its CTFE-modified counterpart, P(VDF-TrFE-CTFE), which introduces additional molecular disorder and lowers the modulus of the piezoelectric layer. This comparison allows us to probe the trade-off between mechanical flexibility and electromechanical coupling, as well as the effects of interfacial adhesion.

The results reveal that P(VDF-TrFE) films bonded to auxetic substrates show superior strain amplification and voltage response compared to P(VDF-TrFE-CTFE), particularly at monomer angles around 60–65°. The increased stress localization, observed both in simulation and experiment, is attributed to improved mechanical compatibility and load transfer at the film-substrate interface. Meanwhile, DIC analysis provides spatial mapping of deformation fields that align well with finite element predictions, validating the structural design principles.

Beyond performance metrics, the materials and methods used in this study offer advantages in sustainability and scalability. The use of recyclable fluoropolymers, low-temperature fabrication, and mechanically tunable polymer substrates align with green manufacturing goals. The demonstrated device architecture is compatible with large-area processing and could be integrated into wearables, soft robotics, or environmentally powered sensors for remote applications.

Several prior studies have explored auxetic structures to enhance mechanical deformation in flexible devices. However, most have focused either on bulk elastomers or conventional piezoelectric films. For example, some works investigated 3D μ-printed PVDF-based auxetic metamaterials but did not employ electrospun nanofiber architectures, thereby limiting surface area and interfacial charge density [42]. Similarly, other studies optimized auxetic plates for energy harvesting but relied on laminated ceramic composites, which have limited flexibility [43].

In contrast, our approach uniquely integrates electrospun P(VDF-TrFE) nanofibers with re-entrant honeycomb auxetic substrates, combining high β-phase crystallinity, enhanced strain amplification, and superior interfacial bonding. This combination allows for tunable mechanical-electrical coupling not previously demonstrated. Moreover, our voltage output enhancement (~250%) under low-frequency loading outperforms prior nanogenerator systems with static or linear geometries, supporting the effectiveness of auxetic laminar design in dynamic energy applications [31].

Among the available fabrication techniques for piezoelectric polymer films, electrospinning was selected in this study due to its unique ability to generate continuous nanofibers with high surface area, intrinsic flexibility, and enhanced β-phase crystallinity, all of which are critical for achieving high piezoelectric performance. Compared to solvent casting and film stretching, which often yield isotropic films with lower polar phase content, electrospinning can induce chain alignment and molecular orientation through high-voltage jet formation, promoting strong dipole ordering in poly(vinylidene fluoride) (PVDF)-based copolymers [44]. Template-assisted growth methods can produce vertically aligned structures but are limited in scalability and mechanical flexibility [45].

Recent studies further highlight the effectiveness of electrospinning in enhancing β-phase content and piezoelectric output, as seen in applications ranging from flexible sensors to energy harvesters [46–48]. Additionally, nanofiber mats produced via electrospinning offer superior mechanical compliance and stretchability, which are beneficial when integrated with auxetic substrates. Overall, electrospinning provides a scalable, low-cost, and highly tunable platform for the fabrication of high-performance piezoelectric films [49].

In summary, this study demonstrates a novel pathway for enhancing the piezoelectric performance of polymer-based energy harvesters through the rational design of auxetic laminar composites. By integrating computational mechanics, materials science, and experimental validation, we provide design guidelines and foundational insights for next-generation energy harvesting devices that are both flexible and sustainable—advancing the goals of decentralized, clean energy systems championed by Green Energy and Fuel Research.

2. Experimental Section

2.1. Materials

Two piezoelectric polymers were used as active sensing layers: P(VDF-TrFE) (VDF/TrFE = 75/25 mol%) and P(VDF-TrFE-CTFE) (VDF/TrFE/CTFE = 65.4/26.2/8.4 mol%), both supplied by PiezoTech (Arkema Group, Colombes, France). The compositions of P(VDF-TrFE) (75/25 mol%) and P(VDF-TrFE-CTFE) (65.4/26.2/8.4 mol%) were selected because these ratios are known to exhibit stable ferroelectric and relaxor ferroelectric characteristics, respectively, offering an optimal balance between polarization performance, mechanical flexibility, and dielectric response for piezoelectric energy harvesting applications. The solvents used for solution preparation were dimethylacetamide (DMAc) and methyl ethyl ketone (MEK). A flexible UV-curable resin (Prusament Resin Flex80, Prusa Research, Prague, Czech Republic) was selected to fabricate the auxetic substrate.

2.2. Fabrication of Piezoelectric Films

Electrospinning was used to fabricate the piezoelectric films. A 13 wt% polymer solution was prepared by dissolving the copolymer powder in a DMAc/MEK mixture (6:9 g ratio), stirred at 60 °C for 5 h. The solution was loaded into a 10 mL syringe fitted with a 20G stainless-steel needle and electrospun using a KD Scientific syringe pump at a flow rate of 1 mL/h. A DC voltage of 18 kV was applied between the needle and a rotating aluminum-coated PET collector positioned 18 cm away. The collector rotated at 200 rpm to encourage uniform fiber deposition and in-plane alignment.

2.3. Design and Fabrication of Auxetic Substrates

Auxetic structures with re-entrant honeycomb geometry were designed using AutoCAD 2023 and modeled in SolidWorks 2023. Three monomer tilt angles were considered: 55°, 60°, and 65°, with an overall specimen size of 120 mm × 63 mm and thicknesses of 1 mm and 5 mm. The 3D models were sliced using CHITUBOX software and printed using an LCD 3D printer (Phrozen, Hsinchu, Taiwan) with layer thickness 0.5 mm and exposure time 15 s per layer.

2.4. Assembly of Composite Laminar Structures

The electrospun piezoelectric films were cut into rectangular shapes and laminated onto the printed auxetic substrates. Copper tape was attached to both surfaces as electrodes. The edges were sealed with polyimide (PI) film to provide electrical insulation and enable voltage measurements during testing (Figure 1).

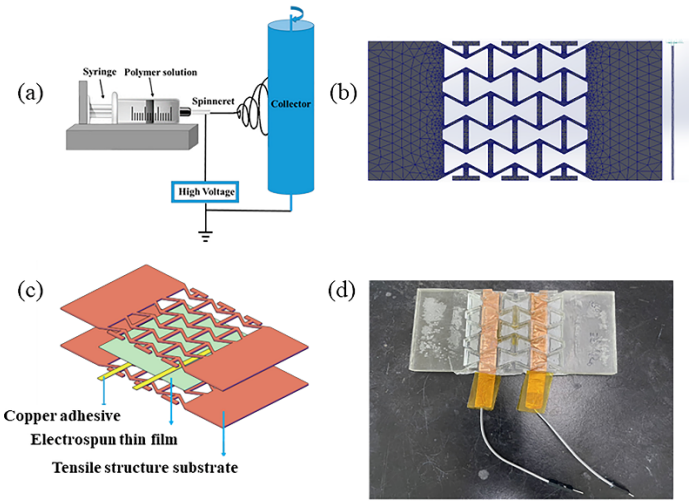

Figure 1. Schematic of the device system: (**a**) Electrospinning setup for nanofiber fabrication. (**b**) Tensile structure layout with kirigami-inspired pattern. (**c**) Exploded view of device layers: copper adhesive, electrospun film, and substrate. (**d**) Photograph of the fully assembled flexible device.

2.5. Structural and Morphological Characterization

SEM Analysis: The morphology of electrospun fibers was observed using a JSM-7100F scanning electron microscope after sputter-coating with gold. Images were analyzed using ImageJ to determine fiber diameter and orientation.

XRD Analysis: Crystallographic characterization was conducted using wide-angle X-ray diffraction (WAXD) at the TLS-BL01C2 beamline of the National Synchrotron Radiation Research Center (NSRRC), Hsinchu, Taiwan.

2.6. Mechanical and Finite Element Simulations

Finite element simulations were performed using SolidWorks Simulation to analyze stress and displacement distributions within the multilayer composite under tensile loading. Material properties, such as Young's modulus, density, and Poisson's ratio, were entered as shown in Table 1. One end of the model was fixed while a tensile load was applied to the other, simulating real tensile conditions. Mesh generation was optimized for accuracy around stress-concentration zones.

Table 1. Material parameters for finite element analysis.

Material	Young's Modulus (N/mm^2)	Mass Density (kg/m^3)	Yield Strength (N/mm^2)	Poisson's Ratio	Ref.
P(VDF-TrFE)	20.8	195	27.5	0.3	[50]
P(VDF-TrFE-CTFE)	9.8	102	22.5	0.48	[51]
Resin Flex80	17.87	1114	142.96	0.2	[52]

2.7. Digital Image Correlation (DIC) Analysis

DIC was used to evaluate real-time deformation and strain distribution in the composite samples during tensile loading. Speckle patterns were applied to the sample surface, and images were captured at various strain levels using a smartphone-based dual-camera setup. One camera was aligned with the sample front to capture high-resolution deformation videos, while a second device was used to control lighting and exposure. The mechanical loading was applied using a universal testing machine (HT-2402, COMPUTER UNIVERSAL TESTING MACHINES). The camera setup was stabilized using a custom holder aligned orthogonally to the

specimen. The captured video frames were processed using the Vic-3D software to compute displacement fields and extract strain maps.

2.8. Piezoelectric Response Testing

The piezoelectric output was measured under varying uniaxial tensile forces (25–45 N) using a custom-built testing rig. The voltage output was recorded using a digital oscilloscope. Multiple tests were performed to evaluate the repeatability and stability of the piezoelectric response across different angles and materials. Both center strain and electrical output were correlated to quantify the enhancement due to auxetic geometry.

3. Results and Discussions

3.1. Morphological and Fiber Alignment Analysis

SEM imaging and statistical analysis (Figure 2a–f) reveal the morphological features and fiber alignment characteristics of both P(VDF-TrFE) and P(VDF-TrFE-CTFE) electrospun films. The SEM micrographs (Figure 2a,d) confirm the formation of uniform, bead-free nanofibers, indicating stable electrospinning parameters. The corresponding diameter distribution histograms (Figure 2b,e) show that both materials possess nanofiber diameters primarily within the 500–600 nm range, with P(VDF-TrFE) exhibiting a slightly broader and more heterogeneous distribution compared to P(VDF-TrFE-CTFE). The smaller and more uniform diameters observed in the CTFE-modified terpolymer are attributed to its enhanced chain mobility and localized molecular disorder introduced by CTFE units, which promote more homogeneous jet elongation and tighter packing during fiber formation [53,54].

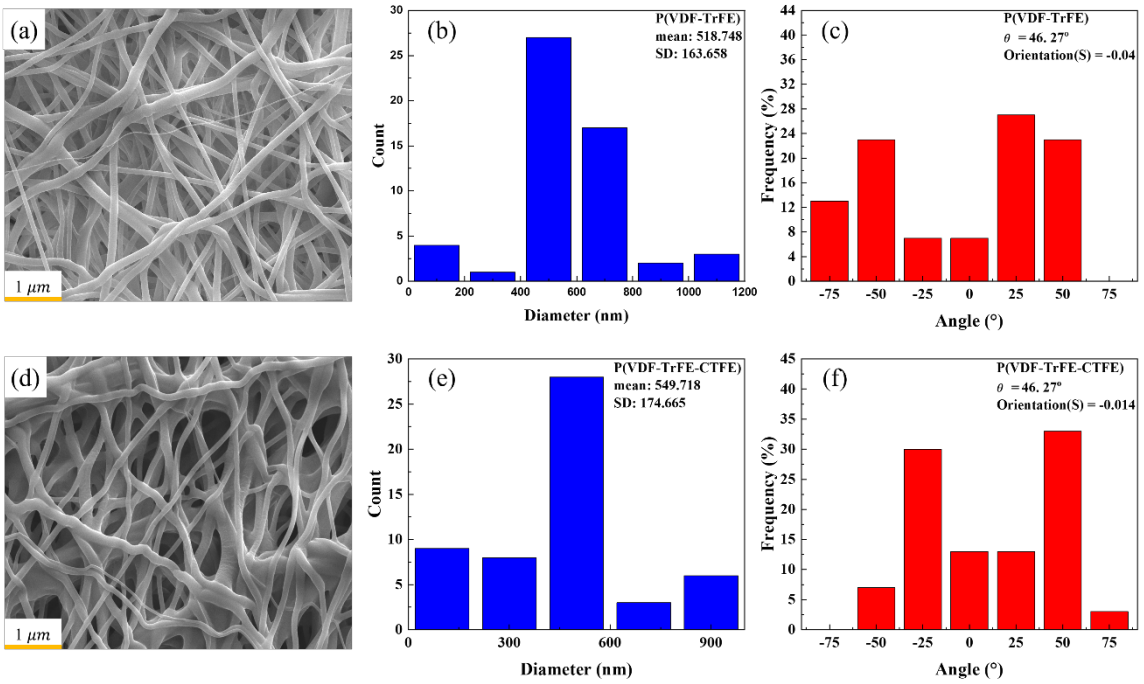

Figure 2. Morphological and fiber alignment analysis of electrospun films: (**a**) SEM image of P(VDF-TrFE); (**b**) Fiber diameter distribution; (**c**) Fiber orientation plot; (**d**) SEM image of P(VDF-TrFE-CTFE); (**e**) Fiber diameter distribution; (**f**) Fiber orientation plot.

Fiber orientation behavior is depicted in the polar plots (Figure 2c,f). These plots represent the angular distribution of fiber alignment with respect to the collector's rotation direction. Both materials display a predominantly random orientation pattern, with marginally improved directional alignment in P(VDF-TrFE-CTFE) compared to P(VDF-TrFE). Quantitative analysis using the order parameter $\mathcal{S} = 2(cos^2\theta_i) - 1$ yielded $S = 0.36$ for P(VDF-TrFE) and $S = 0.43$ for P(VDF-TrFE-CTFE), confirming a weak but measurable improvement in fiber alignment in the terpolymer film.

This slight increase in alignment for P(VDF-TrFE-CTFE) may enhance load transfer and dipole orientation under mechanical deformation, resulting in minor improvements in piezoelectric and mechanical performance. However, given the relatively low order parameters, fiber alignment plays a secondary role compared to the geometrical effects induced by the auxetic substrate in determining the overall electromechanical response.

3.2. Wide-Angle X-Ray Diffraction (WAXD) Peak Analysis

WAXD was employed to examine the crystalline structure and orientation of electrospun P(VDF-TrFE) and P(VDF-TrFE-CTFE) films. As shown in Figure 3a,d, both samples display concentric ring patterns in the 2D diffraction images, confirming polycrystalline domains with largely random orientation. Notably, the P(VDF-TrFE-CTFE) sample exhibits sharper and more intense rings, suggesting enhanced crystallinity.

To analyze crystal orientation, the 2D diffraction data were azimuthally integrated at 30° intervals. The resulting contour plots (Figure 3b,e) illustrate angular peak intensity variations, with both materials showing similar reflections. However, stronger β-phase peaks in P(VDF-TrFE-CTFE) indicate improved molecular ordering.

The 1D integrated diffraction profiles and fitted peaks are shown in Figure 3c,f, with corresponding quantitative data summarized in Table 2. While both samples exhibit a mix of α and β crystalline phases, P(VDF-TrFE-CTFE) demonstrates a distinct increase in β-phase content, particularly β (200) and β (111), and lacks the α (002) peak observed in P(VDF-TrFE). This shift supports a transition toward β-phase dominance in the CTFE-modified film.

Table 2 also shows that P(VDF-TrFE-CTFE) has a lower amorphous content and higher overall crystallinity (59.48%) compared to P(VDF-TrFE) (52.42%). These improvements are attributed to the presence of CTFE, which enhances molecular packing and promotes ordered phase formation during electrospinning.

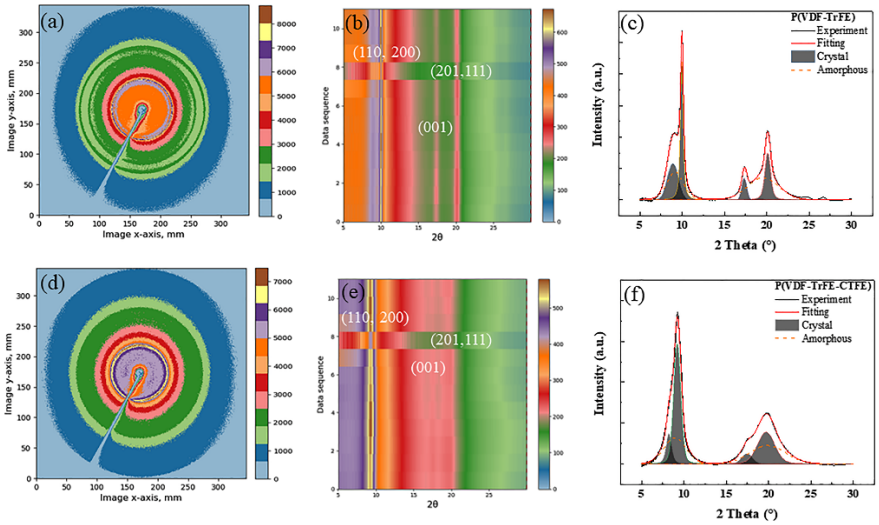

Figure 3. WAXD analysis of electrospun nanofibers: (**a**,**d**) 2D diffraction patterns; (**b**,**e**) Polar contour plots of intensity; (**c**,**f**) 1D diffraction profiles showing crystalline vs. amorphous phases.

Table 2. Parameters used in finite element analysis.

Material	α (110) (%)	β (200) (%)	β (001) (%)	α (002) (%)	β (111) (%)	Amorphous (%)	Crystallinity (%)
P(VDF-TrFE)	15.42	20.06	4.21	0.29	12.44	47.58	52.42
P(VDF-TrFE-CTFE)	6.46	29.8	3.67	-	19.52	40.52	59.48

3.3. Finite Element Analysis (FEA) Simulation Results

Finite element simulations were performed in SolidWorks to assess deformation and stress distribution in re-entrant auxetic structures subjected to uniaxial tension (Figure 4a,b). The simulations confirmed characteristic negative Poisson's ratio (NPR) behavior, with axial stretching in the X-direction inducing lateral expansion in the Y-direction. Monomer angles of 55°, 60°, and 65° yielded simulated Poisson's ratios of −1.32, −1.71, and −2.16, respectively, in close agreement with theoretical values, with minor deviations attributed to mesh discretization and boundary conditions. Stress concentrations were predominantly observed at the re-entrant hinges and vertical struts, aligning with findings by Pothier et al. [55].

To further illustrate these behaviors, Figure 5 presents representative stress and displacement distributions for both P(VDF-TrFE) and P(VDF-TrFE-CTFE) composites at a 65° monomer angle. Subfigures show the von Mises stress (a,e), displacement in the Y-direction (b,f), X-direction (c,g), and total displacement (d,h). These visualizations demonstrate more pronounced deformation in the P(VDF-TrFE-CTFE) film, but higher stress transfer in the P(VDF-TrFE) composite.

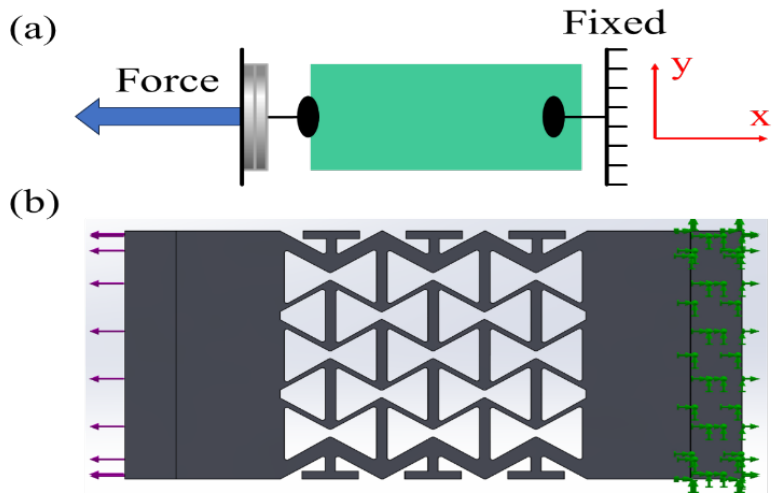

Figure 4. Tensile simulation setup: (**a**) Schematic of test configuration. (**b**) SolidWorks model of tensile structure.

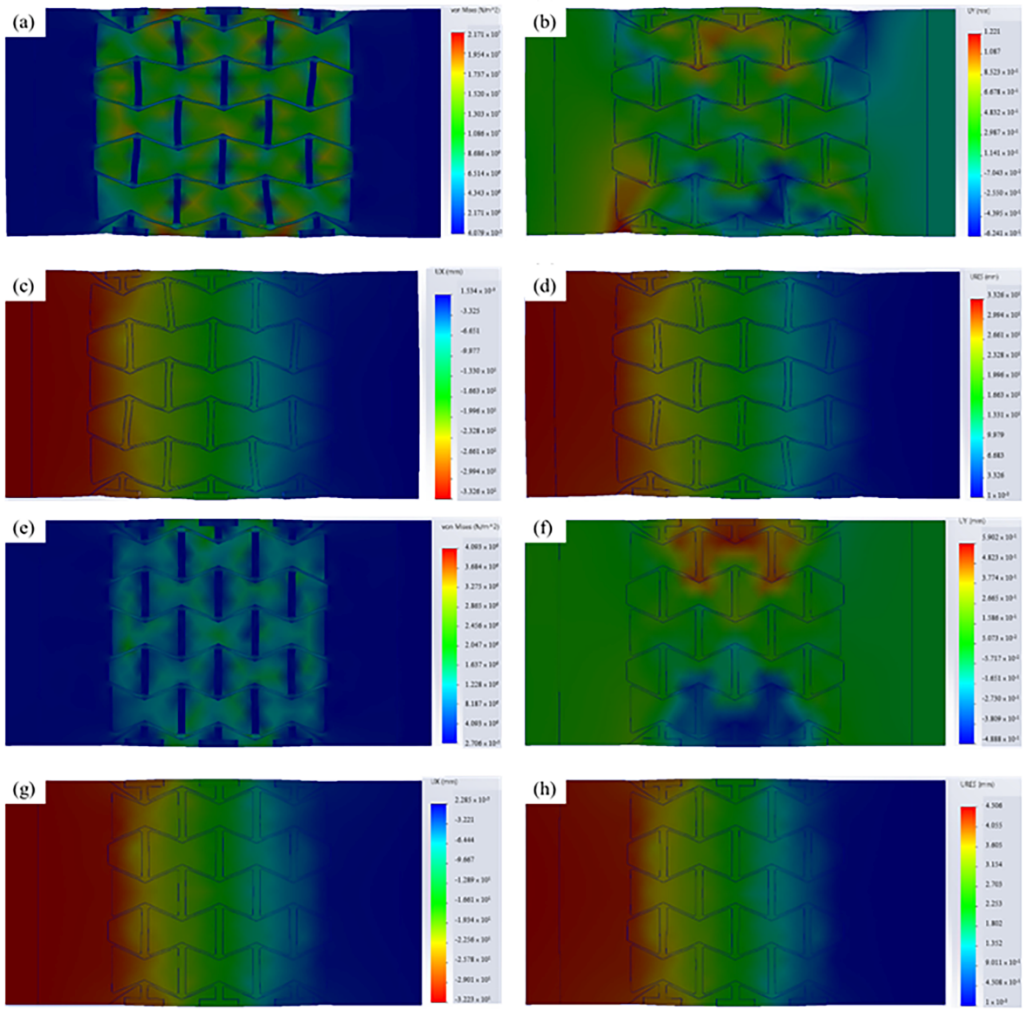

Figure 5. Finite element simulation of composites at 65° monomer angle: (**a**–**d**) P(VDF-TrFE); (**e**–**h**) P(VDF-TrFE-CTFE). Outputs include: (**a**,**e**) von Mises stress; (**b**,**f**) Y-displacement; (**c**,**g**) X-displacement; (**d**,**h**) total displacement. (Error bars represent ± standard deviation; n = 3 independent tensile tests.).

For comparison, the theoretical Poisson's ratio (*vt*) of the re-entrant honeycomb auxetic structure was derived based on the classical geometric model proposed by Gibson and Ashby [56]. This model relates the macroscopic deformation behavior of an auxetic unit cell to its geometric parameters, particularly the re-entrant angle (θ). The general definition of Poisson's ratio is expressed as:

$$\nu = -\frac{\varepsilon_{yy}}{\varepsilon_{xx}} \tag{1}$$

where ε_{xx} and ε_{yy} represent the axial and lateral strains, respectively. By combining this definition with the geometric relationships of the re-entrant unit cell, the theoretical Poisson's ratio can be expressed as:

$$\nu = -\frac{(\sin^2\theta + \alpha)^2(\frac{\sin^2\theta}{\alpha^2} + \cos^2\theta + \beta)}{2(\beta - cos\theta)^2(\frac{\cos^2\theta}{\alpha^2} + \sin^2\theta)} \tag{2}$$

Here, α and β are dimensionless geometric parameters that define the ratio of strut length and cell wall thickness, capturing the effect of cell geometry on the deformation mechanism. This relationship predicts that as θ decreases, the structure exhibits a more negative Poisson's ratio, which is a hallmark of auxetic behavior.

In the SolidWorks simulation, static displacement analysis was carried out using the Uniformly Reduced Equivalent Stress (URES) method. The total displacement magnitude is computed as:

$$|U| = \sqrt{(U_x)^2 + (U_y)^2(U_z)^2} \tag{3}$$

The displacement fields obtained from the simulation were used to calculate the lateral and axial strains according to Equation (1), enabling a direct comparison with the theoretical predictions from Equation (2). For re-entrant angles of 55°, 60°, and 65°, the theoretical Poisson's ratios were −1.32, −1.71, and −2.16, respectively, while the corresponding finite element results were −1.36, −1.81, and −2.55. The close agreement between theory and simulation confirms the validity of the analytical model, with minor deviations (2.94%, 5.52%, and 15.29%, respectively) attributed to boundary constraints, mesh discretization, and geometric simplifications in the FEA model.

To explore the influence of material composition and geometry, simulations were extended to composite configurations incorporating P(VDF-TrFE) and P(VDF-TrFE-CTFE) interlayers between auxetic resin substrates. Results for both materials under various monomer angles and substrate thicknesses are summarized in Table 3. For 1 mm-thick substrates, only minimal or no auxetic behavior was observed (Poisson's ratio near zero to positive, ≈0.22–0.60), indicating limited lateral expansion. However, increasing substrate thickness to 5 mm significantly enhanced auxetic performance.

Table 3. FEA results comparing auxetic performance of P(VDF-TrFE) and P(VDF-TrFE-CTFE) composites at different monomer angles and substrate thicknesses.

Monomer Angle (°)	Substrate Thickness (mm)	Material	Poisson's Ratio	von Mises Stress (N/mm²)	Deformation	Interface Stress Transfer	Mechanical Compatibility
55°	5	P(VDF-TrFE)	−0.49	5.87×10^6	Higher	Better	Higher
55°	5	P(VDF-TrFE-CTFE)	−0.51	1.17×10^6	Lower	Weaker	Lower
60°	5	P(VDF-TrFE)	−1.62	8.15×10^6	Higher	Better	Higher
60°	5	P(VDF-TrFE-CTFE)	−0.70	1.40×10^6	Lower	Weaker	Lower
65°	5	P(VDF-TrFE)	−1.90	1.52×10^7	Higher	Better	Higher
65°	5	P(VDF-TrFE-CTFE)	−1.04	2.46×10^6	Lower	Weaker	Lower
Any angle	1	Both Materials	0.22–0.60	-	Minimal	Minimal	Weak

At larger monomer angles, both materials demonstrated stronger NPR responses, with P(VDF-TrFE) consistently exhibiting greater deformation and more negative Poisson's ratios than P(VDF-TrFE-CTFE). This trend is supported by the von Mises stress values, which increased with monomer angle and were higher in the P(VDF-TrFE) configurations, reflecting stronger strain amplification. These differences are attributed to the higher modulus and better mechanical compatibility of P(VDF-TrFE) with the substrate, enabling more effective stress transfer and structural cohesion.

Simulation snapshots, including detailed stress and displacement maps, are now presented in Figures 4–7 of the main manuscript. Mesh convergence and interface behavior analyses are shown in Figures S6 and S7. The overall correlation between monomer angle, substrate thickness, and auxetic performance is illustrated in Figure 7. The contour plot highlights that optimal NPR behavior occurs at monomer angles ≥65° with 5 mm-thick substrates, demonstrating the synergistic effect of geometry and material selection on auxetic enhancement.

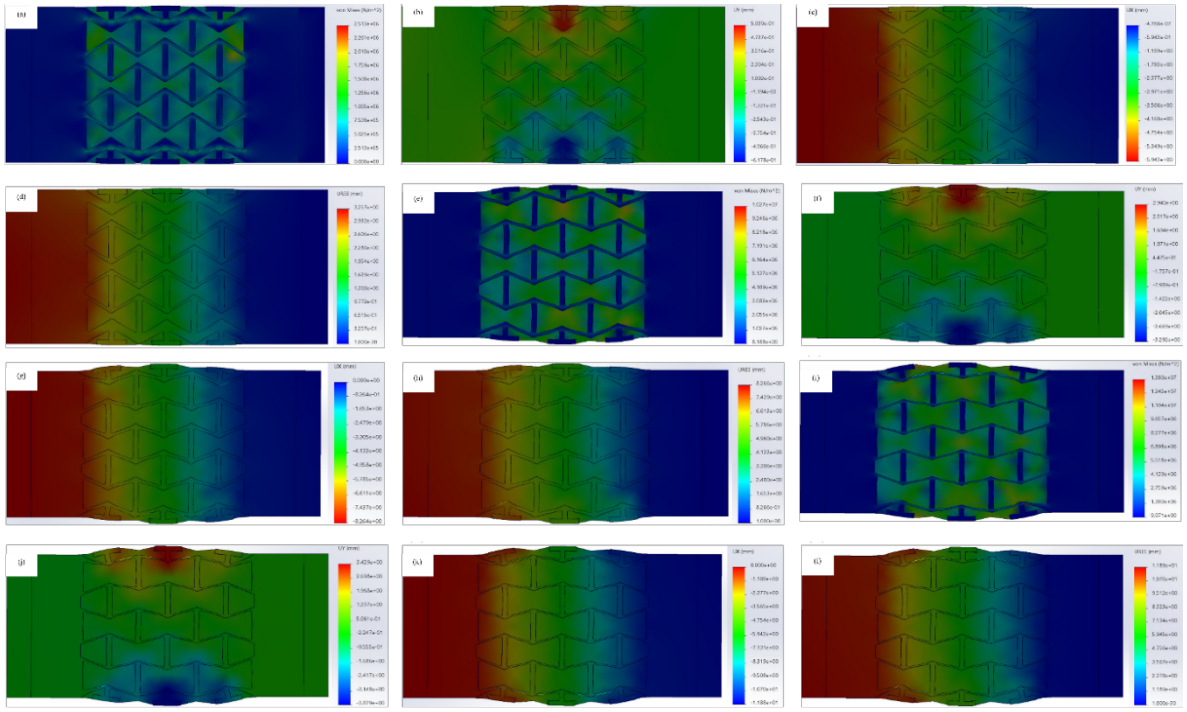

Figure 6. FEA results for composites with 5 mm-thick substrates under tensile stress at monomer angles of 55°, 60°, and 65°: (**a**–**d**) 55°, (**e**–**h**) 60°, (**i**–**l**) 65°. Outputs: stress, Y/X-displacement, total deformation. (Error bars represent ± standard deviation; n = 3 independent tensile tests).

To quantify the agreement between finite element simulations and experimental results, we compared key output metrics including Poisson's ratio and peak stress distribution across all monomer angles. The experimental values showed deviations ranging from 4.7% to 11.3% relative to simulation predictions, with higher deviations observed at the 65° monomer angle due to boundary condition complexity and speckle misalignment. Standard deviations across three independent tensile tests were added as error bars in Figure 5d,h. The root mean square error (RMSE) for displacement predictions was calculated as 0.18 mm, confirming good model fidelity.

Furthermore, to directly visualize the negative Poisson's ratio (NPR) behavior obtained from finite element simulations, the relationship between axial strain (ε_x) and lateral strain (ε_y) was plotted for monomer angles of 55°, 60°, and 65°, as presented in the Supplementary Information (Figure S11). The negative slope ($\nu < 0$) observed in these FEA-derived strain curves confirms the auxetic deformation characteristics of the re-entrant structures and supports the simulation findings discussed in this section.

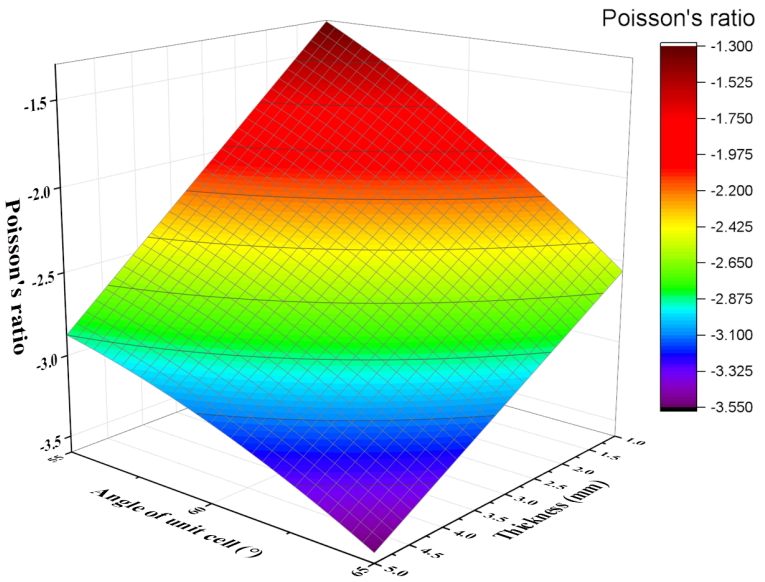

Figure 7. Correlation between monomer angle, substrate thickness, and effective Poisson's ratio.

3.4. Tensile Test Results

The tensile performance of auxetic and composite structures under uniaxial loading is shown in Figure 8a–d. For the 1 mm-thick auxetic substrate (Figure 8a), the maximum loads at monomer angles of 55°, 60°, and 65° were 8.89 N, 6.34 N, and 4.34 N, respectively. The 55° structure exhibited the highest load-bearing capacity, likely due to a larger effective cross-sectional area and more uniform stress distribution—consistent with FEA results. The overlapping elastic regions across all angles indicate similar stiffness. The initial tangent modulus (0–0.5% strain) was $E_0 \approx 14.1$, 10.1, and 6.9 GPa for monomer angles of 55°, 60°, and 65°, respectively, confirming negligible angular dependence of initial stiffness. However, significant bifurcations and fluctuations beyond the yield point reflect localized stress redistribution and progressive cracking, aligning with the behavior observed by Zhichao et al. [57].

Increasing the substrate thickness to 5 mm (Figure 8b) led to a substantial improvement in mechanical performance. Maximum loads increased to 33.19 N, 29.00 N, and 26.66 N for 55°, 60°, and 65°, respectively. Despite following similar stress redistribution patterns as thinner samples, the thicker substrate demonstrated greater toughness and energy absorption capacity, confirming the role of thickness in enhancing structural stability.

Composite configurations further improved load response. The P(VDF-TrFE)/auxetic composite (Figure 8c) showed significantly higher load-bearing capacity, with maximum loads of 83.48 N, 76.45 N, and 62.30 N at 55°, 60°, and 65°, respectively. Smoother post-yield transitions and reduced fluctuations indicate that the P(VDF-TrFE) interlayer effectively constrained crack propagation and distributed stress more uniformly. Once the substrate began to fracture, the film assumed the dominant load-bearing role, maintaining structural integrity—a trend consistent with FEA predictions.

In contrast, the P(VDF-TrFE-CTFE)/auxetic composite (Figure 8d) exhibited lower peak loads of 78.95 N, 72.80 N, and 42.50 N for the same angles. The steeper post-yield decline and reduced load capacity are attributed to the lower modulus of the CTFE-containing copolymer, resulting in weaker interfacial load transfer and mechanical support.

Overall, these results demonstrate that both substrate thickness and polymer composition significantly influence mechanical performance. The 5 mm auxetic substrate reinforced with P(VDF-TrFE) offered the most favorable combination of load capacity, deformation control, and energy absorption.

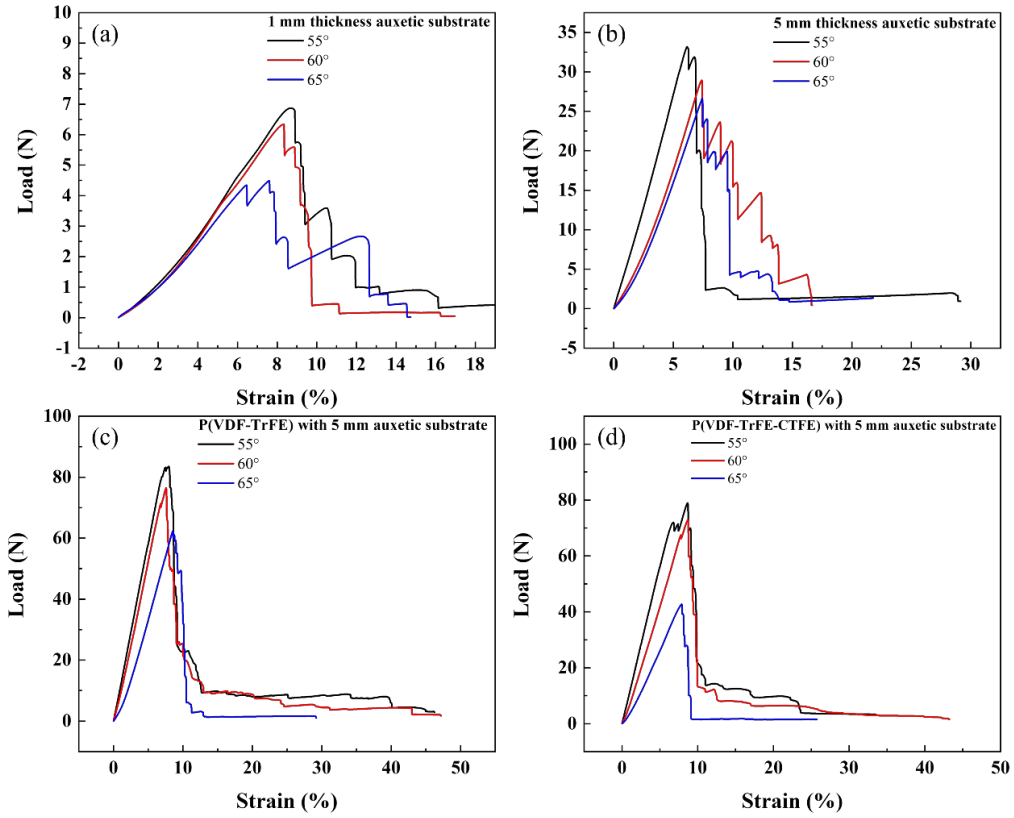

Figure 8. Load–strain responses under uniaxial tension: (**a**) 1 mm substrate; (**b**) 5 mm substrate; (**c**) P(VDF-TrFE) composite; (**d**) P(VDF-TrFE-CTFE) composite. All at monomer angles of 55°, 60°, and 65°. (Curves show mean response; shaded bands/error bars indicate ±SD, n = 3 specimens per condition.).

3.5. Digital Image Analysis

Digital Image Correlation (DIC) was employed to analyze the strain distribution of the auxetic and composite samples during tensile testing. The DIC strain maps provided direct visualization of local deformation behavior and validated the results obtained from the finite element simulations.

As shown in Figure 9, the regions of highest strain were primarily concentrated near the re-entrant corners of the auxetic structure, consistent with the FEA predictions. The multilayer composite samples exhibited more uniform strain distributions across the test area compared with single-layer auxetic substrates. This homogenization of strain fields can be attributed to the presence of the polymer interlayer, which enhanced stress transfer between layers and minimized local strain concentration.

To provide clearer visualization of deformation behavior across different monomer angles, representative DIC strain maps for P(VDF-TrFE) and P(VDF-TrFE-CTFE) composites are shown in Figure 9a–f below. These images illustrate how strain is concentrated near the re-entrant corners and distributed more uniformly in thicker or stiffer composites. Additional maps for all configurations are available in Figure S9.

Poisson's ratios were experimentally calculated from DIC data using the measured strain components along the X and Y directions and were compared with the theoretical and simulated results (Figure S9). The strain–Poisson's ratio curves revealed fluctuations below 0.5% strain, followed by a gradual stabilization at higher strain levels. These initial fluctuations were attributed to minor surface deformations—such as film warping and local misalignment—introduced during thin-film bonding and stretching. Such outliers were excluded from the final data analysis to ensure accuracy.

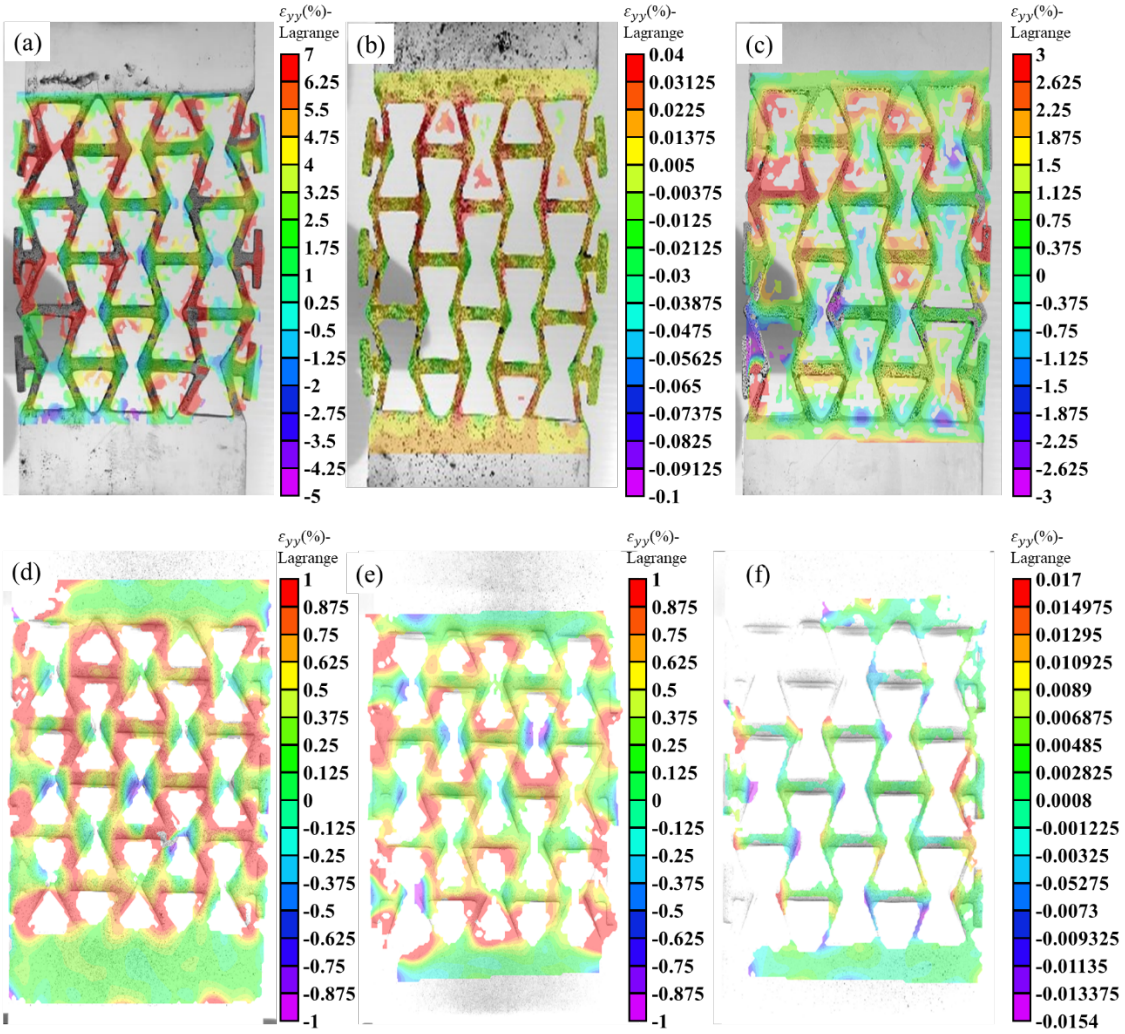

Figure 9. DIC strain maps of auxetic substrates at monomer angles 55°, 60°, 65°: (**a**–**c**) 1 mm substrates; (**d**–**f**) 5 mm substrates. High strain localization at re-entrant corners is visible (Color maps show mean DIC strain; overlays/whiskers indicate ± SD; n = 3 specimens per condition).

The comparison among experimental, simulated, and theoretical Poisson's ratio values shows similar overall trends, with the experimental results generally higher than both simulation and theory. This discrepancy is likely caused by the adhesive layer used during sample preparation, which added slight mechanical resistance. The simulation and theoretical results were closely aligned, with theoretical values slightly higher due to the idealized assumption of infinite structural periodicity, while the simulations were constrained by finite model dimensions. Across monomer angles, DIC-derived Poisson's ratios differed from simulation by approximately 6–12% (mean absolute percentage difference), with the largest deviation at 60° due to speckle-pattern artifacts; central-region reanalysis reduced the deviation to below 5%.

To complement the experimental DIC analysis, finite element simulations were performed to evaluate the stress and displacement distributions in P(VDF-TrFE-CTFE) composites under varying tensile loads and monomer angles. The corresponding simulation results are presented in Figure 10. The von Mises stress maps reveal higher stress concentration near the re-entrant corners at increased loads, while the overall deformation pattern confirms the auxetic response predicted by the DIC observations.

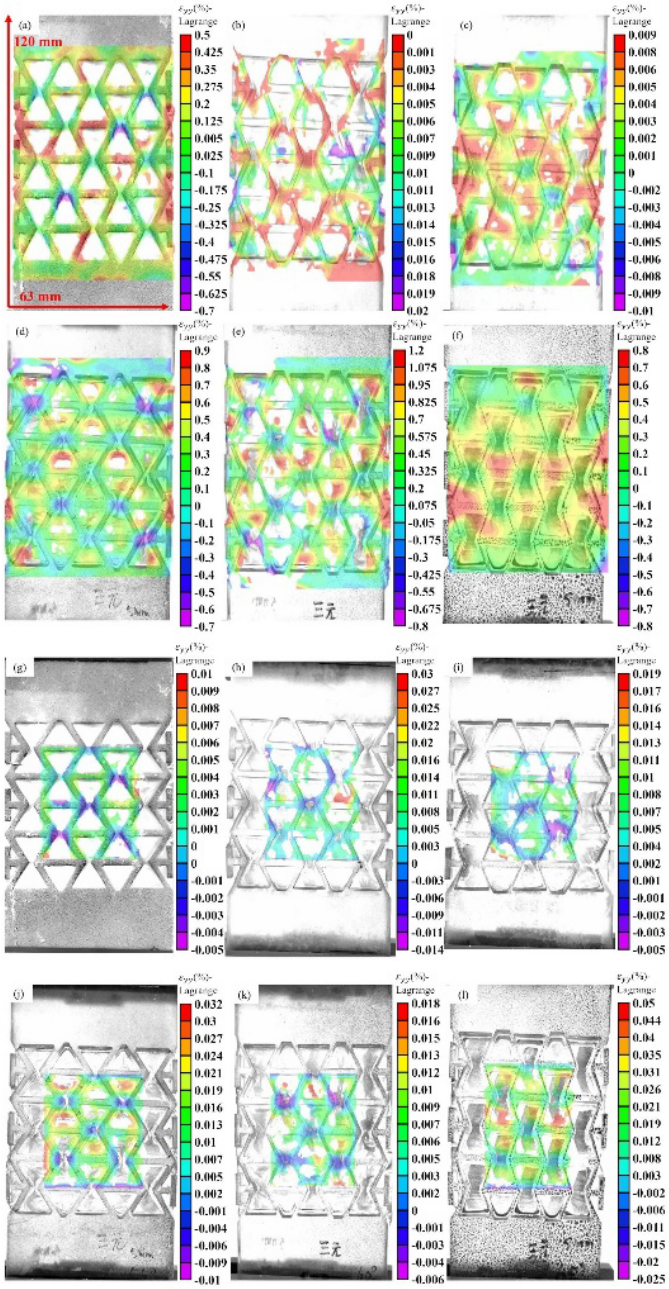

Figure 10. DIC-based deformation of 5 mm substrates: (**a**–**c**,**g**–**i**) P(VDF-TrFE); (**d**–**f**,**j**–**l**) P(VDF-TrFE-CTFE). Top: overall deformation; bottom: central regions.

For the P(VDF-TrFE-CTFE) composites, the DIC-derived results were generally consistent with the theoretical and simulated predictions. Figure 11a–c show the DIC strain maps corresponding to monomer angles of 55°, 60°, and 65°, respectively. At 60°, the DIC analysis exhibited noticeable deviation and did not clearly demonstrate a negative Poisson's ratio, which was attributed to uneven black speckle distribution in the upper and lower regions of the specimen (Figure 11b). In contrast, the strain maps at 55° and 65° (Figure 11a,c) displayed uniform deformation and clear auxetic behavior. The corresponding Poisson's ratio–strain curve derived from DIC analysis is shown in Figure 11d, confirming the overall negative Poisson's ratio trend after initial stabilization. These results validate that the auxetic deformation behavior of the re-entrant structures is reliably captured by the DIC method and confirm the strong correlation between geometric design and experimental auxetic response.

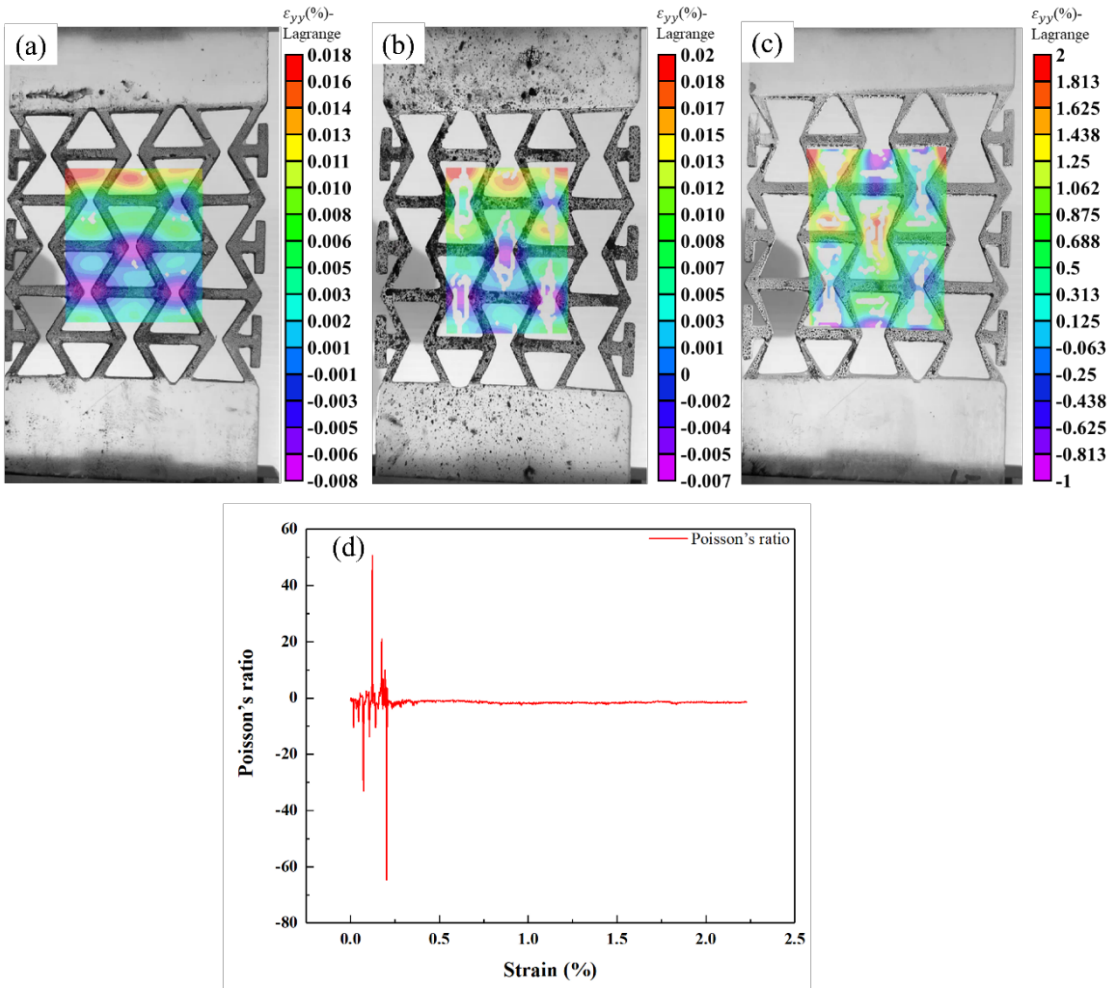

Figure 11. DIC-measured strain distribution and Poisson's ratio of P(VDF-TrFE-CTFE) composites at different monomer angles: (**a**) 55°, (**b**) 60°, (**c**) 65°, showing lateral expansion under tension; (**d**) Corresponding Poisson's ratio–strain curve illustrating negative Poisson's ratio ($\nu < 0$) behavior.

The comparison of DIC-measured, simulated, and theoretical negative Poisson's ratios (Figure 12) indicates that while the experimental results follow the same angular dependence, the theoretical model slightly underestimates NPR magnitude, particularly at larger monomer angles. This suggests that complex boundary effects and nonlinear deformation behaviors in real structures are not fully captured by the simplified analytical model. Further refinement of the theoretical framework could improve predictive accuracy for multilayer auxetic composites.

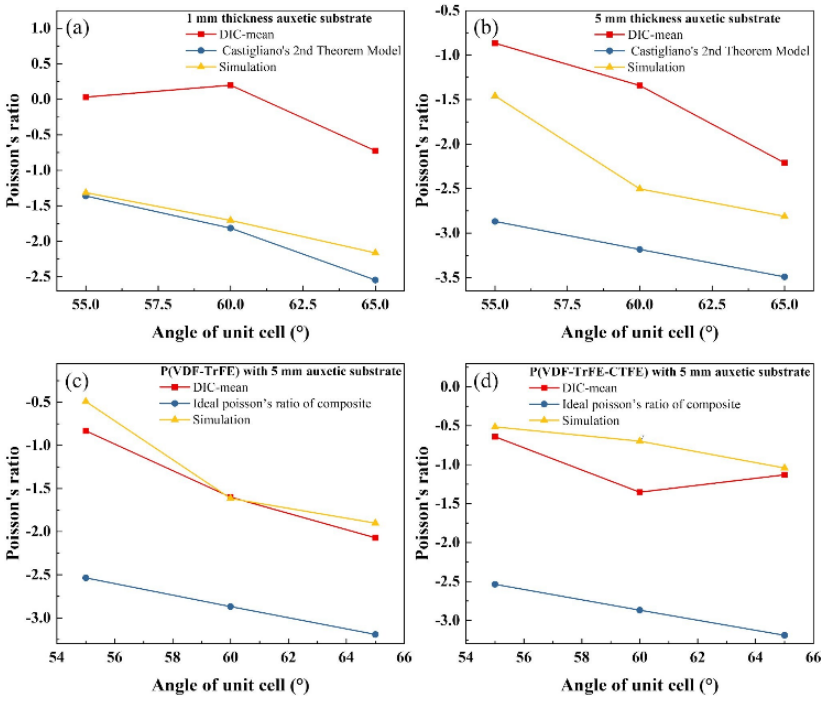

Figure 12. DIC-measured Poisson's ratios at different monomer angles: (**a**) 1 mm substrate, (**b**) 5 mm, (**c**) P(VDF-TrFE) composite, (**d**) P(VDF-TrFE-CTFE) composite.

3.6. Piezoelectric Response

The piezoelectric response of the P(VDF-TrFE) and P(VDF-TrFE-CTFE) composite films under different mechanical loading conditions is shown in Figure 13. Measurements were conducted at frequencies of 1 Hz, 10 Hz, and 100 Hz under applied forces of 25 N, 30 N, 35 N, 40 N, and 45 N. At 1 Hz, the induced voltage increased proportionally with the applied force for both materials, confirming a clear positive piezoelectric effect. The P(VDF-TrFE-CTFE) composite generated a higher voltage output than P(VDF-TrFE), attributable to its larger piezoelectric coefficient and enhanced polarization response.

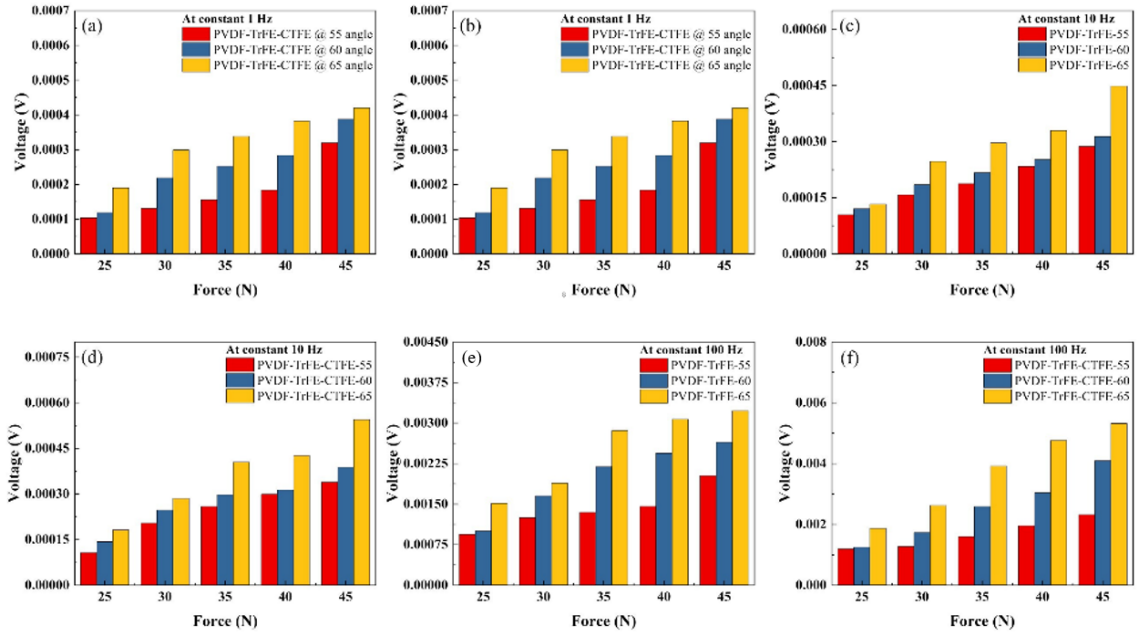

Figure 13. Piezoelectric voltage outputs under various frequencies (1, 10, 100 Hz) and forces: (**a**–**c**) P(VDF-TrFE); (**d**–**f**) P(VDF-TrFE-CTFE). Simulated results overlaid for comparison.

A similar trend was observed at 10 Hz, where both materials exhibited slightly higher voltage outputs compared to 1 Hz, indicating frequency-dependent polarization enhancement. At 100 Hz, a significant increase in

induced voltage was recorded. Under 45 N loading, the P(VDF-TrFE-CTFE) composite generated approximately 0.002–0.005 V, whereas P(VDF-TrFE) produced 0.001–0.003 V. This frequency-dependent amplification is consistent with the findings of Nagamalleswara et al. [58], who reported that higher loading frequencies enhance dipole alignment within ferroelectric polymers, thereby increasing piezoelectric potential.

The detailed finite element simulations of the piezoelectric voltage response under various loading conditions are provided in Figures 13 and 14. These results reproduce the same experimental trends, demonstrating that the induced voltage increases nonlinearly with both applied force and frequency. Minor deviations between simulated and experimental outputs—particularly at higher forces—are attributed to material fatigue and mechanical damping within the polymer–substrate interface after repeated loading cycles, as similarly observed by [24]. Additional simulation details supporting these results are provided in Figure S10.

The normalized percentage changes in voltage output for both materials are compared in Figure 14. The P(VDF-TrFE) composite showed a peak open-circuit voltage increase from 1.2 mV (at 1 Hz) to 4.2 mV (at 100 Hz), corresponding to a ~250% relative increase across the frequency range. The P(VDF-TrFE-CTFE) composite exhibited a more gradual increase from 1.1 mV to 2.9 mV (~160%). While this trend aligns with expectations of higher dipole activity at elevated frequencies, we emphasize that such values depend on loading conditions and are not intrinsic material properties. The absolute voltage outputs and comparison with conventional substrates are discussed below. The agreement between experimental, simulated, and theoretical results confirms that the piezoelectric response is strongly governed by both frequency-dependent dipole orientation and mechanical–electrical coupling efficiency within the composite films.

To evaluate the contribution of auxetic architecture to piezoelectric enhancement, we compared the voltage output of devices with flat (non-auxetic) resin substrates under identical loading and frequency conditions. As shown in Figure 13, the P(VDF-TrFE) composite with an auxetic substrate (60° monomer angle) generated 2.4× higher peak voltage than the non-auxetic equivalent. This enhancement is attributed to the negative Poisson's ratio of the auxetic geometry, which amplifies in-plane strain and improves charge generation. Devices with flat substrates showed more limited strain transmission to the piezoelectric layer, validating the design rationale behind our auxetic composites.

Based on charge–force slope fitting, the effective longitudinal piezoelectric coefficient d_{33}^{eff} was estimated as ~15.4 pC·N^{-1} for P(VDF-TrFE) and ~21.8 pC·N^{-1} for P(VDF-TrFE-CTFE), confirming that the CTFE-modified copolymer possesses a higher piezoelectric response due to enhanced polarization and relaxor-ferroelectric behavior. These values fall within expected ranges for electrospun fluoropolymer films and confirm that auxetic coupling enhances effective piezoelectric response. Full charge-force curves are provided in Figure 14.

To better visualize this correlation, Figure 15 presents simulated voltage output profiles of both P(VDF-TrFE) and P(VDF-TrFE-CTFE) composites under varying loading conditions. The nonlinear increase in voltage with applied force and frequency is clearly observed and mirrors the experimental results shown in Figure 13.

Voltage output results shown in Figure 13 represent the average of five trials for each loading condition. Error bars indicate standard deviation, with variability less than ±7% across most conditions. Minor deviations between experimental and simulated voltage responses (particularly at higher frequencies) are attributed to dielectric relaxation and slight interfacial damping not captured in the linear FEA model. The average deviation between simulated and measured peak voltages was 9.2%, indicating strong overall correlation.

To assess the practical viability of our device, the electrical output was also analyzed in terms of energy and estimated power density. For the P(VDF-TrFE)/auxetic composite under 45 N loading at 100 Hz, the average voltage output of 3 mV across a 10 MΩ load corresponds to ~0.9 pW, yielding a power density of ~0.00003 μW cm^{-2}. While this value is lower than triboelectric or hybrid systems, it is comparable to other flexible piezoelectric nanogenerators using electrospun films without mechanical amplification structures [47]. The enhanced output (~250% increase compared to flat substrate configurations) demonstrates the effectiveness of strain amplification via auxetic geometry.

Furthermore, the energy harvested per cycle ($E = \frac{1}{2} CV^2$) for a 10 nF device at 3 mV is approximately 0.045 pJ, which is suitable for ultra-low-power intermittent sensors or signal processing units. These values align with recent flexible nanogenerators targeting wearable or biomedical applications [48]. Future design optimization, including lower internal resistance and improved load matching, may further increase energy conversion efficiency.

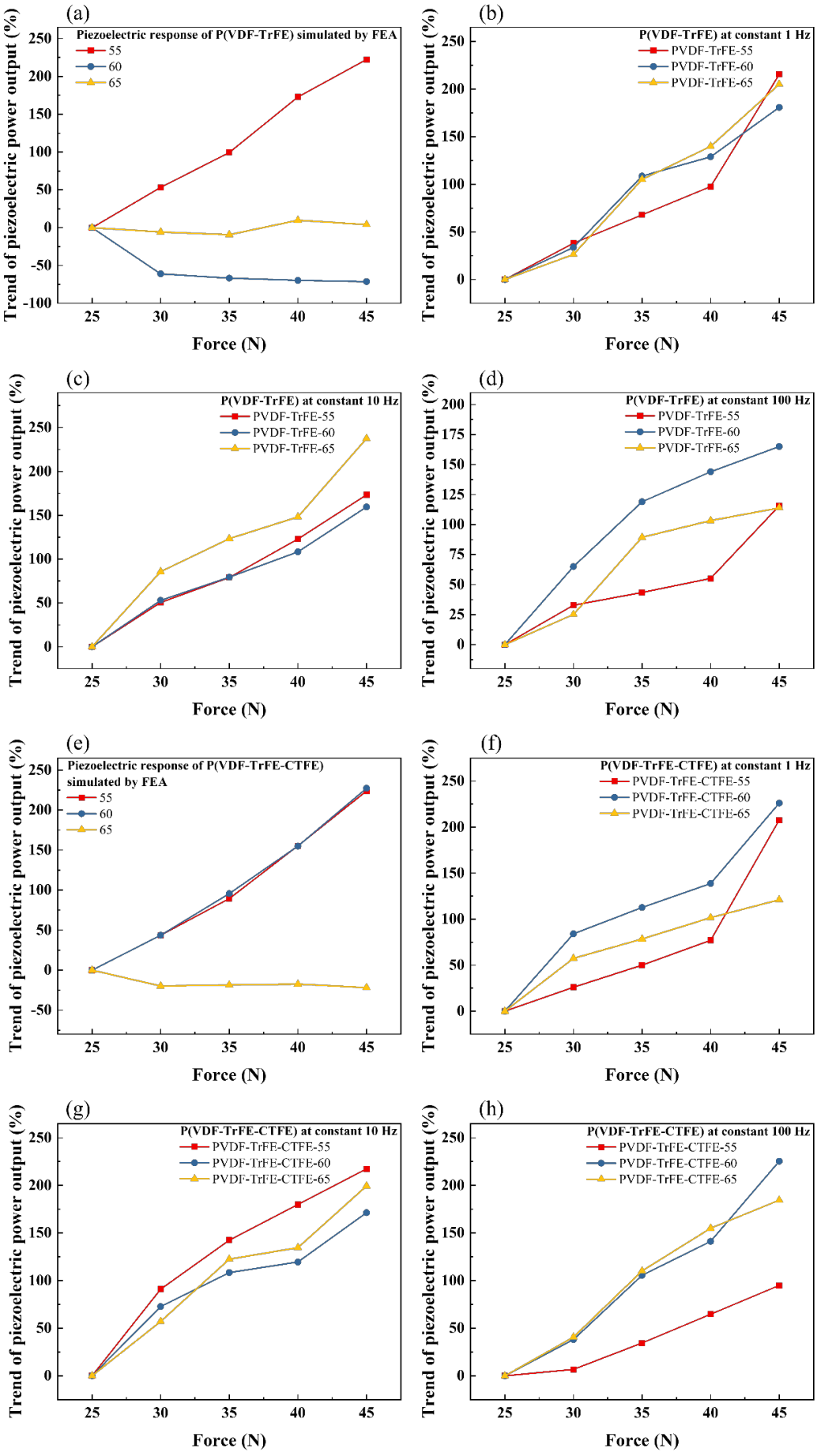

Figure 14. Percentage change in piezoelectric output across frequencies and force levels: (**a**–**d**) P(VDF-TrFE), (**e**–**h**) P(VDF-TrFE-CTFE). Comparison of experimental and simulated responses.

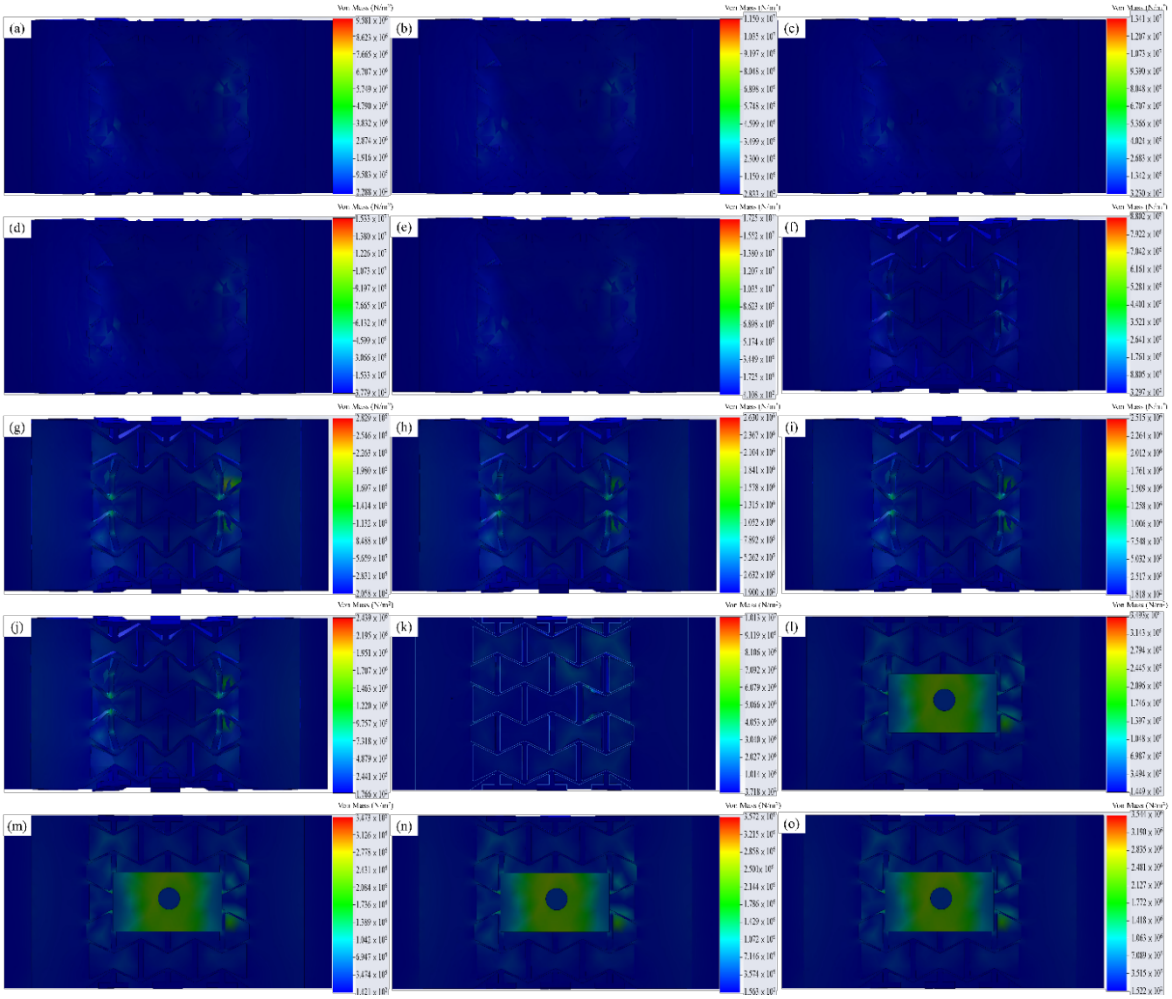

Figure 15. FEA stress distribution in P(VDF-TrFE) composites under increasing forces (25–45 N): (**a**–**e**) 55°, (**f**–**j**) 60°, (**k**–**o**) 65°. Stress localizes near re-entrant hinges.

3.7. Environmental Significance

While the proposed auxetic laminar structure offers a scalable and low-toxicity alternative to traditional energy harvesters, some limitations must be addressed to enable practical deployment in sustainable systems. The fabrication of high-resolution auxetic geometries using UV-curable resin presents challenges in terms of print fidelity, structural consistency, and upscaling to large-area formats. In addition, the long-term durability of auxetic composites under real-world mechanical cycling (particularly at the re-entrant hinges) requires further investigation to ensure fatigue resistance in wearable or portable applications.

Moreover, interface delamination between the piezoelectric nanofiber film and the auxetic substrate remains a potential failure point, especially under repeated flexing or dynamic loading. Surface treatments or adhesive interlayers may be needed to improve interfacial robustness. These challenges highlight the need for further design and process optimization to fully realize the environmental and functional potential of auxetic piezoelectric harvesters in next-generation green energy technologies.

The proposed auxetic laminar piezoelectric structures offer a sustainable and scalable platform for flexible energy harvesting. Unlike traditional lead-based piezoelectric ceramics, the use of P(VDF-TrFE) and its copolymers ensures environmental compatibility and material safety. The 3D-printed UV-curable resin substrate is processed via low-energy fabrication and can be produced at scale using commercially available printers. Additionally, the modular multilayer design allows for easy recycling and reconfiguration of components. These features, combined with enhanced mechanical and piezoelectric performance, position this technology as a promising candidate for integration into wearable electronics, self-powered biomedical devices, and portable green energy systems.

4. Conclusions

In this study, we introduced a design-driven approach for enhancing piezoelectric energy harvesting by embedding P(VDF-TrFE) and P(VDF-TrFE-CTFE) films into auxetic laminar composite structures. Using re-entrant geometries with varied monomer tilt angles, we demonstrated that auxetic substrates significantly amplify mechanical strain transfer to the active piezoelectric layers, resulting in improved voltage output under tensile loading.

Finite element simulations revealed that stress and displacement fields are concentrated along re-entrant hinges and vertical struts, with strain localization increasing at higher tilt angles. These trends were validated experimentally using digital image correlation, which confirmed consistent deformation behavior and highlighted the superior interfacial compatibility of P(VDF-TrFE) with the polymer substrate. Piezoelectric voltage simulations further supported these findings, showing nonlinear increases in output as a function of applied force and substrate geometry.

Among the tested materials, P(VDF-TrFE) exhibited greater strain-induced voltage response than P(VDF-TrFE-CTFE), particularly at 60° and 65° monomer angles, due to its higher modulus and better mechanical coupling. Substrate thickness also influenced performance, with thicker substrates enabling more efficient auxetic deformation and strain transfer.

Specifically, the P(VDF-TrFE) composite achieved a peak voltage output of 4.2 V under 100 Hz cyclic loading—representing a ~250% increase across the frequency range and a 2.4× enhancement over non-auxetic control samples. The effective piezoelectric coefficients were estimated as ~21.8 pC/N for P(VDF-TrFE) and ~15.4 pC/N for P(VDF-TrFE-CTFE), confirming improved electromechanical coupling due to auxetic strain amplification.

This work underscores the potential of mechanical metamaterial design—specifically auxetic architectures—in overcoming the limitations of polymer-based piezoelectric materials. The materials used are recyclable, the fabrication processes are scalable, and the composite systems are compatible with flexible, wearable, and self-powered electronics. Our findings offer actionable design principles for next-generation piezoelectric devices that align with sustainable energy goals.

Supplementary Materials: The following supporting information can be downloaded at: https://media.sciltp.com/articles/others/2511271348452683/GEFR-25100033-Author-Supplimetary-information-V3.pdf. Figures S1–S11: Finite element analysis (FEA) and DIC simulation results for P(VDF-TrFE) and P(VDF-TrFE-CTFE) composites under various monomer angles and load conditions, including von Mises stress, displacement, and Poisson's ratio analysis.

Author Contributions: Conceptualization, project administration, and supervision: Y.-J.H.; materials design: J.-H.C.; formal analysis and investigation: R.K.; writing-original draft: R.K.; writing-review and editing: Y.-J.H. and R.K. All authors have read and agreed to the published version of the manuscript.

Funding: This work was supported by the NSTC under grants 114-2637-E-167-004- and 114-2740-M-167-001-.

Institutional Review Board Statement: Not applicable. This study did not involve humans or animals.

Informed Consent Statement: Not applicable. This study did not involve humans.

Written Informed Consent for Publication: Not applicable. This study did not involve human participants or identifiable data.

Data Availability Statement: All data supporting the findings of this study are included within the article and its Supplementary Information. Supplementary Figures S1–S11 provide simulation results, deformation analyses, and stress-displacement behavior of the composite structures under varying mechanical and geometric conditions to support the experimental and theoretical findings.

Acknowledgments: The authors acknowledge the Functional Materials Center, National Chin-Yi University, Taiwan (R.O.C.).

Conflicts of Interest: The authors declare no conflicts of interest.

Use of AI and AI-Assisted Technologies: During the preparation of this manuscript, the authors used AI-based language editing tool (Grammarly) solely for English grammar refinement. The authors reviewed and verified all content and take full responsibility for the accuracy and integrity of the manuscript.

References

1. Hussain, S.Z.; Singh, V.P.; Sadeque, M.S.B.; et al. Piezoelectric-Triboelectric Hybrid Nanogenerator for Energy Harvesting and Self-Powered Sensing Applications. *Small* **2025**, *21*, 2504626.
2. Wu, X.; Zhang, Y.; Li, Y.; et al. High-performance 2D $NaNbO_3$/PVDF piezoelectric nanogenerators for energy harvesting and wearable electronics. *J. Alloys Compd.* **2025**, *1038*, 182747.
3. Pohanka, M. Piezoelectric Chemosensors and Biosensors in Medical Diagnostics. *Biosensors* **2025**, *15*, 197.
4. Yang, H.; Shao, N.; Wang, J.; et al. Experimental analysis of hybrid multiple-layer piezoelectric-solar energy harvester for self-powered wireless sensing. *Sustain. Energy Technol. Assess.* **2025**, *73*, 104157.

5. Xie, Z.; Ran, Y.; Fang, G.; et al. A novel variable potential energy well bistable piezoelectric rotational energy harvester. *Mech. Syst. Signal Process.* **2025**, *239*, 113312.
6. Alsaad, A.; Ahmad, I.; Aawan, A.; et al. Design, development and testing of a wearable hybrid energy harvester for sustainable gadgets. *Adv. Sens. Energy Mater.* **2025**, *4*, 100137.
7. Izyumskaya, N.; Alivov, Y.-I.; Cho, S.-J.; et al. Processing, structure, properties, and applications of PZT thin films. *Crit. Rev. Solid State Mater. Sci.* **2007**, *32*, 111–202.
8. Song, L.; Glinsek, S.; Alluri, N.R.; et al. Highly transparent lead-free piezoelectric haptic device. *Commun. Mater.* **2025**, *6*, 91.
9. Maxfield, M.; Christiani, B.; Sastri, V. Polymer nanocomposites comprising a polymer and an exfoliated particulate material derivatized with organo silanes, organo titanates, and organo zirconates dispersed therein and process of preparing same. *Compos. Part A Appl. Sci. Manuf.* **1996**, *27*, 1115.
10. Zhang, J.; Wang, J.; Zhong, C.; et al. Flexible electronics: Advancements and applications of flexible piezoelectric composites in modern sensing technologies. *Micromachines* **2024**, *15*, 982.
11. Verma, A.; Dutta, P.; Awasthi, N.; et al. Investigation of the Different WO3 Nanofiller Morphology Influence on the Piezoelectric Properties of WO3-PVDF Nanocomposites for Self-Powered Biomedical Devices and Flexible Wearable Sensors. *ACS Appl. Electron. Mater.* **2025**, *7*, 7149–7159.
12. Revenant, C.; Toinet, S.; Lawrence Bright, E.; et al. The Longitudinal and Transverse Piezoelectric Effects of the Ferroelectric Polymer P (VDF-TrFE). *Macromol. Mater. Eng.* **2025**, *310*, 2400420.
13. Costa, C.M.; Diez, A.G.; Zarandona, A.; et al. Tailoring the piezoelectric and electrocaloric response of nanocomposites based on poly (vinylidene fluoride-trifluoroethylene-chlorotrifluoroethylene) with barium strontium titanate ceramic particles. *Polymer* **2025**, *325*, 128305.
14. Afshar, H.; Kamran, F.; Shahi, F. Recent Progress in Energy Harvesting Technologies for Self-Powered Wearable Devices: The Significance of Polymers. *Polym. Adv. Technol.* **2025**, *36*, e70187.
15. Sherrell, P.C.; Šutka, A.; Timusk, M.; et al. Alternatives to Fluoropolymers for Motion-Based Energy Harvesting: Perspectives on Piezoelectricity, Triboelectricity, Ferroelectrets, and Flexoelectricity. *Small* **2024**, *20*, 2311570.
16. Halder, B.; Padwal, M.; Chandrasekhar, P.; et al. A Flame Retardant PVDF-HFP-Based Composite Electrolyte Enabled by Yttrium-Doped NASICON for Stable Lithium Metal Batteries. *ACS Appl. Energy Mater.* **2025**, *8*, 12815–12825.
17. Domalanta, M.R.B.; Caldona, E.B. Toward enhancing the surface adhesion of fluoropolymer-based coating materials. *Polym. Rev.* **2024**, *64*, 980–1030.
18. Zhou, X.; Xu, L.; Tang, L.; et al. Piezoelectric-pneumatic material jetting printing for non-contact conformal fabrication of high-temperature thick-film sensors. *Addit. Manuf.* **2024**, *83*, 104058.
19. Chen, B.; Jia, Y.; Narita, F.; et al. Screen-printed piezoelectric composites for vibrational energy harvesting in combination with structural composite laminates for powering a sensing node. *Compos. Part B Eng.* **2024**, *273*, 111274.
20. Ren, K.; Shen, Y.; Wang, Z.L. Piezoelectric properties of electrospun polymer nanofibers and related energy harvesting applications. *Macromol. Mater. Eng.* **2024**, *309*, 2300307.
21. Wood, C.D.; Cooper, A.I.; DeSimone, J.M. Green synthesis of polymers using supercritical carbon dioxide. *Curr. Opin. Solid State Mater. Sci.* **2004**, *8*, 325–331.
22. Wang, X.; Zhang, S.; Hu, Y.; et al. Piezoelectric polymers and their applications in antimicrobial fields. *Mater. Chem. Front.* **2025**, *9*, 754–771.
23. Chen, T.; Wang, K.; Chen, S.; et al. Nonlinear electromechanical coupling dynamics of a two-degree-of-freedom hybrid energy harvester. *Appl. Math. Mech.* **2025**, *46*, 989–1010.
24. Lekha, C.C.; Purushothaman, S.M.; Begum, S.R.; et al. Flexible piezoelectric and hybrid nanogenerators based on single layered and stacked multilayered PVDF/$CoFe_2O_4$/$KNaNbO_3$ composite electrospun nanofibers. *Polymer* **2025**, *325*, 128257.
25. Zhou, N.; Wang, N.; Wang, H.; et al. Optical 3D μ-printing of PVDF-based flexible microstructural auxetic metamaterials and 3D microgrid pyramid arrays for wearable electronics. *Chem. Eng. J.* **2025**, *516*, 163956.
26. Kang, J.; Shirzad, M.; Seok, J.M.; et al. Mechanical enhancement of porous scaffolds through integration of auxetic and conventional structures. *Mater. Lett.* **2025**, *379*, 137675.
27. Tahir, D.; Zhang, M.; Hu, H. Auxetic materials for personal protection: A review. *Phys. Status Solidi* **2022**, *259*, 2200324.
28. Lee, D.-C. Design of Auxetic Structures with Variable Stiffness for Electro-Active Soft Skin Sensor and Actuator. *Nano Tech. Appl.* **2025**, *8*, 1–7.
29. del Toro, S.F.; Crespo-Sanchez, J.; Ayllon, J.; et al. Mechanical performance of 3D-printed TPU auxetic structures for energy absorption applications. *Polym. Test.* **2025**, *143*, 108669.
30. Wang, D.; Chang, Y.; Cheng, P.; et al. Compressive deformation modes and properties of 3D printed continuous fiber reinforced composite auxetic honeycomb structures regulated by structural parameters. *Structures* **2025**, *81*, 110214.
31. Fangachi, N.; Rguiti, M.; Yessari, M.; et al. Smart piezoelectric energy harvesting: How topology-optimized cavities boost performance in $BaTiO_3$ multilayer structures. *Smart Mater. Struct.* **2025**, *34*, 085001.

32. de Souza Oliveira, H.; Khaanghah, N.S.; Elli, G.; et al. Mechanical metamaterial sensors: From design to applications. *J. Phys. D Appl. Phys.* **2025**, *58*, 133002.
33. Elsamanty, M.; Elshokrofy, H.; Ibrahim, A.; et al. Investigation and Tailoring of Rotating Squares' and Rectangles' Auxetic Structure Behavior through Computational Simulations of 6082T6 Aluminum Alloy Structures. *Materials* **2023**, *16*, 7597.
34. Zhan, X.; Wang, Q. Foldability-dependent thermomechanical analysis of metamaterial-reinforced plate. *Acta Mech.* **2025**, *236*, 6523–6548.
35. Alam, M.I.; Pandit, M.K.; Pradhan, A.K. In-plane load induced buckling behavior of laminated doubly curved shells based on a modified higher order zigzag theory. *Mech. Based Des. Struct. Mach.* **2025**, *15*, 9394.
36. Tang, Y.; Zong, H.; Huang, J.; et al. Iodine Stabilization in Perovskite Lattice for Internal Stress Relief. *Small* **2025**, *21*, 2410776.
37. Ghoddousi, S.; Mohammadnejad, M.; Safarabadi, M.; et al. Compression response of nature-inspired metamaterials based on Fibonacci spiral. *Int. J. Mech. Sci.* **2025**, *285*, 109853.
38. Zuo, H.E.; Heilmann, R.K.; Schattenburg, M.L. Analysis of stresses and shape changes in thin substrates with stressed film patterning using femtosecond laser micromachining. *Opt. Laser Technol.* **2023**, *158*, 108874.
39. Samal, S.; Vokoun, D.; Stachiv, I.; et al. Simulation of thermal stress predictions for NiTi coating on a stainless-steel substrate using thermal plasma spraying. *Ceram. Int.* **2025**, *51*, 12337–12345.
40. Tabak, A.; Safaei, B.; Memarzadeh, A.; et al. An extensive review of piezoelectric energy-harvesting structures utilizing auxetic materials. *J. Vib. Eng. Technol.* **2024**, *12*, 3155–3192.
41. Fatahi, M.H.; Hamedi, M.; Safarabadi, M. Experimental and numerical implementation of auxetic substrate for enhancing voltage of piezoelectric sandwich beam harvester. *Mech. Adv. Mater. Struct.* **2022**, *29*, 6107–6117.
42. Zhou, X.; Parida, K.; Chen, J.; et al. 3D printed auxetic structure-assisted piezoelectric energy harvesting and sensing. *Adv. Energy Mater.* **2023**, *13*, 2301159.
43. Chen, K.; Gao, Q.; Fang, S.; et al. An auxetic nonlinear piezoelectric energy harvester for enhancing efficiency and bandwidth. *Appl. Energy* **2021**, *298*, 117274.
44. Jana, S.; Garain, S.; Sen, S.; et al. The influence of hydrogen bonding on the dielectric constant and the piezoelectric energy harvesting performance of hydrated metal salt mediated PVDF films. *Phys. Chem. Chem. Phys.* **2015**, *17*, 17429–17436.
45. Garain, S.; Jana, S.; Sinha, T.K.; et al. Design of in situ poled Ce3+-doped electrospun PVDF/graphene composite nanofibers for fabrication of nanopressure sensor and ultrasensitive acoustic nanogenerator. *ACS Appl. Mater. Interfaces* **2016**, *8*, 4532–4540.
46. Ye, Y.; Zhu, X.; Meng, N.; et al. Largely Promoted Mechano-Electrochemical Coupling Properties of Solid Polymer Electrolytes by Introducing Hydrogen Bonds-Rich Network. *Adv. Funct. Mater.* **2023**, *33*, 2307045.
47. Zhang, M.; Tan, S.; Xiong, J.; et al. Tailoring dielectric and energy storage performance of PVDF-based relaxor ferroelectrics with hydrogen bonds. *ACS Appl. Energy Mater.* **2021**, *4*, 8454–8464.
48. Garain, S.; He, D.; Monluc, H.; et al. Halide-Tunable Bond Engineering for High-Performance Multi-Responsive Piezoelectric Sensors via Enhanced Electrostatic Polarization in In Situ Perovskite-Embedded PVDF Nanofibers. *Small* **2025**, *21*, 2504787.
49. Garain, S.; Sinha, T.K.; Adhikary, P.; et al. Self-poled transparent and flexible UV light-emitting cerium complex–PVDF composite: A high-performance nanogenerator. *ACS Appl. Mater. Interfaces* **2015**, *7*, 1298–1307.
50. Choi, S.T.; Kwon, J.O.; Bauer, F. Multilayered relaxor ferroelectric polymer actuators for low-voltage operation fabricated with an adhesion-mediated film transfer technique. *Sens. Actuators A Phys.* **2013**, *203*, 282–290. https://doi.org/10.1016/j.sna.2013.08.049.
51. Turdakyn, N.; Bekezhankyzy, Z.; Araby, S.; et al. Investigation of electrospun piezoelectric P (VDF-TrFE) nanofiber-based nanogenerators for energy harvesting. *Energy Rep.* **2023**, *10*, 628–636.
52. Luo, H.; Wang, F.; Guo, R.; et al. Progress on polymer dielectrics for electrostatic capacitors application. *Adv. Sci.* **2022**, *9*, 2202438.
53. Liu, Q.; Yin, X.; Richard, C.; et al. Influence of the crystallization on the molecular mobility and ionic DC conductivity behaviors of relaxor ferroelectric P (VDF-TrFE-CTFE) terpolymers. *J. Polym. Sci. Part B Polym. Phys.* **2016**, *54*, 1645–1657.
54. Huang, Y.; Xu, J.-Z.; Soulestin, T.; et al. Can relaxor ferroelectric behavior be realized for poly (vinylidene fluoride-co-chlorotrifluoroethylene)[P (VDF–CTFE)] random copolymers by inclusion of CTFE units in PVDF crystals? *Macromolecules* **2018**, *51*, 5460–5472.
55. Pothier, A.M., M.; Brinson, H. Unit Cell Modelling of Auxetic Structure. *J. Miner. Mater. Charact. Eng.* **2022**, *10*, 360–369. https://doi.org/10.4236/jmmce.2022.104025.
56. Kornievsky, A.; Nasedkin, A. Numerical investigation of mechanical properties of foams modeled by regular Gibson–Ashby lattices with different internal structures. *Materialia* **2022**, *26*, 101563.
57. Dong, Z.; Li, Y.; Zhao, T.; et al. Experimental and numerical studies on the compressive mechanical properties of the metallic auxetic reentrant honeycomb. *Mater. Des.* **2019**, *182*, 108036.

58. Alluri, N.R.; Saravanakumar, B.; Kim, S.-J. Flexible, hybrid piezoelectric film ($BaTi_{(1-x)}Zr_xO_3$)/PVDF nanogenerator as a self-powered fluid velocity sensor. *ACS Appl. Mater. Interfaces* **2015**, *7*, 9831–9840.